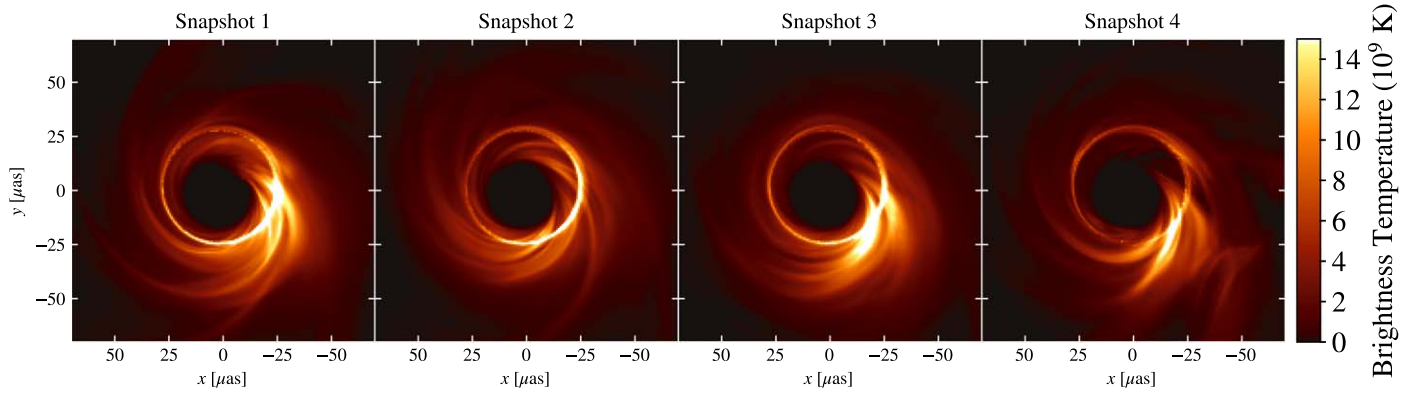

Figure 17. 230 GHz full-resolution snapshots from a fiducial model in the best-bet region. This model passes 10/11 constraints. The different panels are snapshots taken from the "best time," when the synthetic observation has good (u, v) coverage.

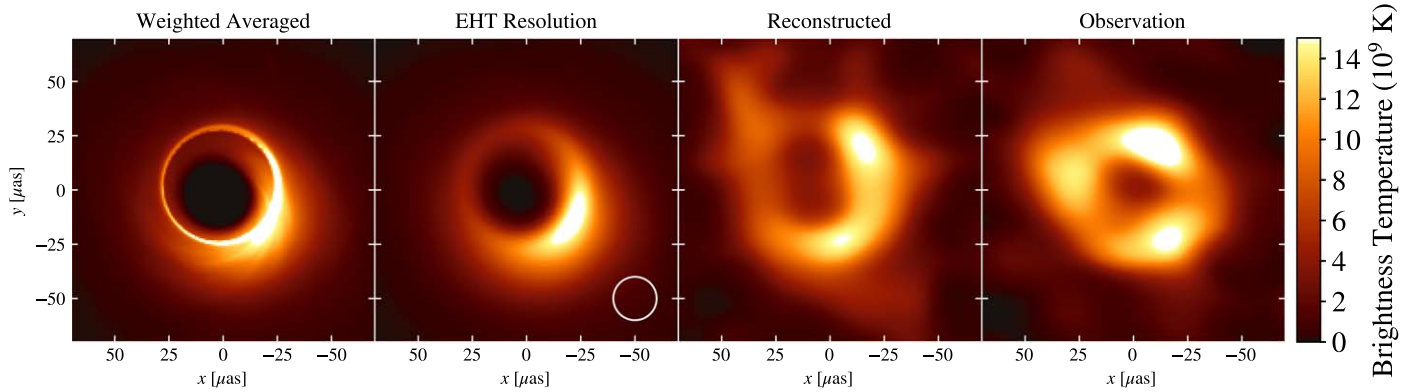

Figure 18. Reconstructions of a fiducial model in the best-bet region, compared to the April 7 observation. This is the same model shown in Figure 17. The leftmost panel shows an average of the snapshots used in the synthetic observation, weighted by the number of baselines at each time. The second panel shows the averaged image convolved with a 20 μas beam, which roughly approximates EHT resolution. The third panel shows an average image reconstructed from synthetic data using the fiducial model. The final image shows the average image reconstructed from April 7 EHT data.

accretion model that follows plasma over a larger range in radius than our fiducial models. It is also an open question whether the outflow power could be detected in the dense but crowded galactic center environment. Notice that this outflow luminosity is comparable to the spin-down luminosity of the Crab pulsar.

All fiducial models assume a particular parameterization for the eDF (the $R_{\rm high}$ prescription), use a common initial setup (a magnetized torus), and assume that the black hole spin vector and torus orbital angular momentum are aligned or anti-aligned. To partially control for the errors introduced by these assumptions, we have included a set of exploratory models. These include several eDF prescriptions, a wind-fed model that tracks accretion from stellar winds down to the scale of the horizon, and tilted disk models in which the black hole spin and torus angular momentum are misaligned.

Our nonthermal models are remarkably similar to their thermal counterparts. For the limited set of nonthermal eDF prescriptions we consider here the 230 GHz image structure differs very little for models in which the nonthermal electrons are introduced mainly in the jet. The 230 GHz variability is not detectably different than corresponding thermal models.[164] The 86 GHz size and flux density, which are the most restrictive non-EHT constraints, are not detectably affected by the addition of nonthermal electrons for most nonthermal models (except $\kappa = 5$ models). Nonthermal electrons consistently increase the 2.2 μm flux density over similar thermal models, however. Accelerating even a small fraction of the electron population into a nonthermal tail risks overproducing 2.2 μm emission. The 2.2 μm (and submm through mid-IR) flux density therefore provides the strongest eDF constraints. Future EHT analyses would benefit from incorporating submm constraints (e.g., Bower et al. 2019), and because model submm SEDs are highly variable, the submm and 2.2 μm data should be as close to simultaneous as possible.

The stellar-wind-fed models of Ressler et al. (2020b) feature the best-motivated treatment of boundary and initial conditions for Sgr A* models. They differ from our torus-initialized fiducial models in that they follow plasma from its ejection from stars on known orbits down to the event horizon. We have imaged these models using an $R_{\rm high}$ prescription for the electron temperature, with $R_{\rm high}$ adjusted in the otherwise parameter-free models to produce the correct time-averaged 230 GHz flux density. The two models considered here, both with $a_* = 0$, fail the 86 GHz flux, m-ring width, and M_3 constraints. This does *not* imply that wind-fed models are ruled out; they clearly merit further investigation with longer integrations over a broader range of eDFs and a_*.

In general, black hole accretion flows can be tilted in the sense that the orbital angular momentum of the disk and the spin angular momentum of the hole are misaligned. Tilted disks

[164] The nonthermal models are imaged over $5 \times 10^3 GM/c^3$, so constraints on M_3 are weaker than for the fiducial models, which are imaged for 3 times as long.

have not until now been included in EHT analyses because (i) it is conceivable that accretion flows align either by consistently oriented long-term accretion or by some analog of the Bardeen −Petterson effect (Bardeen & Petterson 1975) and (ii) the tilted disk parameter space is larger than the aligned disk parameter space by two dimensions: the tilt angle and the longitude of the observer. We considered models with tilt 30° and 60°, observed at a single longitude. The integrations were too short ($3000\,GM/c^3$) to provide strong constraints on tilt, but we find that the m-ring width test is particularly sensitive to tilt and rejects a progressively larger fraction of the models as tilt increases at the single observing longitude studied here. Tilted models clearly merit further investigation.

Our fiducial models and variable κ nonthermal models have been run with independent GRMHD codes and imaged with independent radiative transfer codes. The outcomes are largely consistent (see Appendix A for details). The code comparisons were valuable and helped identify multiple issues in the independent simulation sets. The consistency between codes is remarkable given the complexity of the modeling process and the scope for error. Tracking down the remaining discrepancies (e.g., in the 2.2 μm flux density) and developing a quantitative error budget is an essential but difficult task for the future.

This paper is dedicated to the memory of John F. Hawley, whose pioneering work on black hole accretion flows made this paper possible. We are grateful to an anonymous referee whose comments significantly improved this paper.

The Event Horizon Telescope Collaboration thanks the following organizations and programs: the Academia Sinica; the Academy of Finland (projects 274477, 284495, 312496, 315721); the Agencia Nacional de Investigación y Desarrollo (ANID), Chile via NCN19_058 (TITANs) and Fondecyt 1221421, the Alexander von Humboldt Stiftung; an Alfred P. Sloan Research Fellowship; Allegro, the European ALMA Regional Centre node in the Netherlands, the NL astronomy research network NOVA and the astronomy institutes of the University of Amsterdam, Leiden University and Radboud University; the ALMA North America Development Fund; the Black Hole Initiative, which is funded by grants from the John Templeton Foundation and the Gordon and Betty Moore Foundation (although the opinions expressed in this work are those of the author(s) and do not necessarily reflect the views of these Foundations); Chandra DD7-18089X and TM6-17006X; the China Scholarship Council; China Postdoctoral Science Foundation fellowship (2020M671266); Consejo Nacional de Ciencia y Tecnología (CONACYT, Mexico, projects U0004-246083, U0004-259839, F0003-272050, M0037-279006, F0003-281692, 104497, 275201, 263356); the Consejería de Economía, Conocimiento, Empresas y Universidad of the Junta de Andalucía (grant P18-FR-1769), the Consejo Superior de Investigaciones Científicas (grant 2019AEP112); the Delaney Family via the Delaney Family John A. Wheeler Chair at Perimeter Institute; Dirección General de Asuntos del Personal Académico-Universidad Nacional Autónoma de México (DGAPA-UNAM, projects IN112417 and IN112820); the Dutch Organization for Scientific Research (NWO) VICI award (grant 639.043.513) and grant OCENW.KLEIN.113; the Dutch National Supercomputers, Cartesius and Snellius (NWO Grant 2021.013); the EACOA Fellowship awarded by the East Asia Core Observatories Association, which consists of the Academia Sinica Institute of Astronomy and Astrophysics, the National Astronomical Observatory of Japan, Center for Astronomical Mega-Science, Chinese Academy of Sciences, and the Korea Astronomy and Space Science Institute; the European Research Council (ERC) Synergy Grant "BlackHoleCam: Imaging the Event Horizon of Black Holes" (grant 610058); the European Union Horizon 2020 research and innovation programme under grant agreements RadioNet (No 730562) and M2FINDERS (No 101018682); the Generalitat Valenciana postdoctoral grant APOSTD/2018/177 and GenT Program (project CIDEGENT/2018/021); MICINN Research Project PID2019-108995GB-C22; the European Research Council for advanced grant 'JETSET: Launching, propagation and emission of relativistic jets from binary mergers and across mass scales' (Grant No. 884631); the Institute for Advanced Study; the Istituto Nazionale di Fisica Nucleare (INFN) sezione di Napoli, iniziative specifiche TEONGRAV; the International Max Planck Research School for Astronomy and Astrophysics at the Universities of Bonn and Cologne; DFG research grant "Jet physics on horizon scales and beyond" (Grant No. FR 4069/2-1); Joint Princeton/Flatiron and Joint Columbia/Flatiron Postdoctoral Fellowships, research at the Flatiron Institute is supported by the Simons Foundation; the Japan Ministry of Education, Culture, Sports, Science and Technology (MEXT; grant JPMXP1020200109); the Japanese Government (Monbukagakusho: MEXT) Scholarship; the Japan Society for the Promotion of Science (JSPS) Grant-in-Aid for JSPS Research Fellowship (JP17J08829); the Joint Institute for Computational Fundamental Science, Japan; the Key Research Program of Frontier Sciences, Chinese Academy of Sciences (CAS, grants QYZDJ-SSW-SLH057, QYZDJSSW-SYS008, ZDBS-LY-SLH011); the Leverhulme Trust Early Career Research Fellowship; the Max-Planck-Gesellschaft (MPG); the Max Planck Partner Group of the MPG and the CAS; the MEXT/JSPS KAKENHI (grants 18KK0090, JP21H01137, JP18H03721, JP18K13594, 18K03709, JP19K14761, 18H01245, 25120007); the Malaysian Fundamental Research Grant Scheme (FRGS) FRGS/1/2019/STG02/UM/02/6; the MIT International Science and Technology Initiatives (MISTI) Funds; the Ministry of Science and Technology (MOST) of Taiwan (103-2119-M-001-010-MY2, 105-2112-M-001-025-MY3, 105-2119-M-001-042, 106-2112-M-001-011, 106-2119-M-001-013, 106-2119-M-001-027, 106-2923-M-001-005, 107-2119-M-001-017, 107-2119-M-001-020, 107-2119-M-001-041, 107-2119-M-110-005, 107-2923-M-001-009, 108-2112-M-001-048, 108-2112-M-001-051, 108-2923-M-001-002, 109-2112-M-001-025, 109-2124-M-001-005, 109-2923-M-001-001, 110-2112-M-003-007-MY2, 110-2112-M-001-033, 110-2124-M-001-007, and 110-2923-M-001-001); the Ministry of Education (MoE) of Taiwan Yushan Young Scholar Program; the Physics Division, National Center for Theoretical Sciences of Taiwan; the National Aeronautics and Space Administration (NASA, Fermi Guest Investigator grant 80NSSC20K1567, NASA Astrophysics Theory Program grant 80NSSC20K0527, NASA NuSTAR award 80NSSC20K0645); NASA Hubble Fellowship grant HST-HF2-51431.001-A awarded by the Space Telescope Science Institute, which is operated by the Association of Universities for Research in Astronomy, Inc., for NASA, under contract NAS5-26555; the National Institute of Natural Sciences (NINS) of Japan; the National Key Research and Development Program of China (grant 2016YFA0400704, 2017YFA0402703, 2016YFA0400702); the National Science

Foundation (NSF, grants AST-0096454, AST-0352953, AST-0521233, AST-0705062, AST-0905844, AST-0922984, AST-1126433, AST-1140030, DGE-1144085, AST-1207704, AST-1207730, AST-1207752, MRI-1228509, OPP-1248097, AST-1310896, AST-1440254, AST-1555365, AST-1614868, AST-1615796, AST-1715061, AST-1716327, AST-1716536, OISE-1743747, AST-1816420, AST-1935980, AST-2034306); NSF Astronomy and Astrophysics Postdoctoral Fellowship (AST-1903847); the Natural Science Foundation of China (grants 11650110427, 10625314, 11721303, 11725312, 11873028, 11933007, 11991052, 11991053, 12192220, 12192223); the Natural Sciences and Engineering Research Council of Canada (NSERC, including a Discovery Grant and the NSERC Alexander Graham Bell Canada Graduate Scholarships-Doctoral Program); the National Youth Thousand Talents Program of China; the National Research Foundation of Korea (the Global PhD Fellowship Grant: grants NRF-2015H1A2A1033752, the Korea Research Fellowship Program: NRF-2015H1D3A1066561, Brain Pool Program: 2019H1D3A1A01102564, Basic Research Support Grant 2019R1F1A1059721, 2021R1A6A3A01086420, 2022R1C1C1005255); Netherlands Research School for Astronomy (NOVA) Virtual Institute of Accretion (VIA) postdoctoral fellowships; Onsala Space Observatory (OSO) national infrastructure, for the provisioning of its facilities/observational support (OSO receives funding through the Swedish Research Council under grant 2017-00648); the Perimeter Institute for Theoretical Physics (research at Perimeter Institute is supported by the Government of Canada through the Department of Innovation, Science and Economic Development and by the Province of Ontario through the Ministry of Research, Innovation and Science); the Spanish Ministerio de Ciencia e Innovación (grants PGC2018-098915-B-C21, AYA2016-80889-P, PID2019-108995GB-C21, PID2020-117404GB-C21); the University of Pretoria for financial aid in the provision of the new Cluster Server nodes and SuperMicro (USA) for a SEEDING GRANT approved towards these nodes in 2020; the Shanghai Pilot Program for Basic Research, Chinese Academy of Science, Shanghai Branch (JCYJ-SHFY-2021-013); the State Agency for Research of the Spanish MCIU through the "Center of Excellence Severo Ochoa" award for the Instituto de Astrofísica de Andalucía (SEV-2017- 0709); the Spinoza Prize SPI 78-409; the South African Research Chairs Initiative, through the South African Radio Astronomy Observatory (SARAO, grant ID 77948), which is a facility of the National Research Foundation (NRF), an agency of the Department of Science and Innovation (DSI) of South Africa; the Toray Science Foundation; Swedish Research Council (VR); the US Department of Energy (USDOE) through the Los Alamos National Laboratory (operated by Triad National Security, LLC, for the National Nuclear Security Administration of the USDOE (Contract 89233218CNA000001); and the YCAA Prize Postdoctoral Fellowship.

We thank the staff at the participating observatories, correlation centers, and institutions for their enthusiastic support. This paper makes use of the following ALMA data: ADS/JAO. ALMA#2016.1.01154.V. ALMA is a partnership of the European Southern Observatory (ESO; Europe, representing its member states), NSF, and National Institutes of Natural Sciences of Japan, together with National Research Council (Canada), Ministry of Science and Technology (MOST; Taiwan), Academia Sinica Institute of Astronomy and Astrophysics (ASIAA; Taiwan), and Korea Astronomy and Space Science Institute (KASI; Republic of Korea), in cooperation with the Republic of Chile. The Joint ALMA Observatory is operated by ESO, Associated Universities, Inc. (AUI)/NRAO, and the National Astronomical Observatory of Japan (NAOJ). The NRAO is a facility of the NSF operated under cooperative agreement by AUI. This research used resources of the Oak Ridge Leadership Computing Facility at the Oak Ridge National Laboratory, which is supported by the Office of Science of the U.S. Department of Energy under Contract No. DE-AC05-00OR22725. We also thank the Center for Computational Astrophysics, National Astronomical Observatory of Japan. The computing cluster of Shanghai VLBI correlator supported by the Special Fund for Astronomy from the Ministry of Finance in China is acknowledged.

APEX is a collaboration between the Max-Planck-Institut für Radioastronomie (Germany), ESO, and the Onsala Space Observatory (Sweden). The SMA is a joint project between the SAO and ASIAA and is funded by the Smithsonian Institution and the Academia Sinica. The JCMT is operated by the East Asian Observatory on behalf of the NAOJ, ASIAA, and KASI, as well as the Ministry of Finance of China, Chinese Academy of Sciences, and the National Key Research and Development Program (No. 2017YFA0402700) of China and Natural Science Foundation of China grant 11873028. Additional funding support for the JCMT is provided by the Science and Technologies Facility Council (UK) and participating universities in the UK and Canada. The LMT is a project operated by the Instituto Nacional de Astrófisica, Óptica, y Electrónica (Mexico) and the University of Massachusetts at Amherst (USA). The IRAM 30-m telescope on Pico Veleta, Spain is operated by IRAM and supported by CNRS (Centre National de la Recherche Scientifique, France), MPG (Max-Planck-Gesellschaft, Germany) and IGN (Instituto Geográfico Nacional, Spain). The SMT is operated by the Arizona Radio Observatory, a part of the Steward Observatory of the University of Arizona, with financial support of operations from the State of Arizona and financial support for instrumentation development from the NSF. Support for SPT participation in the EHT is provided by the National Science Foundation through award OPP-1852617 to the University of Chicago. Partial support is also provided by the Kavli Institute of Cosmological Physics at the University of Chicago. The SPT hydrogen maser was provided on loan from the GLT, courtesy of ASIAA.

This work used the Extreme Science and Engineering Discovery Environment (XSEDE), supported by NSF grant ACI-1548562, and CyVerse, supported by NSF grants DBI-0735191, DBI-1265383, and DBI-1743442. XSEDE Stampede2 resource at TACC was allocated through TG-AST170024 and TG-AST080026N. XSEDE JetStream resource at PTI and TACC was allocated through AST170028. This research is part of the Frontera computing project at the Texas Advanced Computing Center through the Frontera Large-Scale Community Partnerships allocation AST20023. Frontera is made possible by National Science Foundation award OAC-1818253. This research was carried out using resources provided by the Open Science Grid, which is supported by the National Science Foundation and the U.S. Department of Energy Office of Science. Additional work used ABACUS2.0, which is part of the eScience center at Southern Denmark University. Simulations were also performed on the SuperMUC cluster at the LRZ in Garching, on the LOEWE cluster in CSC in Frankfurt, on the HazelHen cluster at the HLRS in Stuttgart, and on the Pi2.0 and Siyuan Mark-I at Shanghai Jiao Tong University. The computer resources of the Finnish IT Center for Science (CSC) and the Finnish

Computing Competence Infrastructure (FCCI) project are acknowledged. This research was enabled in part by support provided by Compute Ontario (http://computeontario.ca), Calcul Quebec (http://www.calculquebec.ca) and Compute Canada (http://www.computecanada.ca).

The EHTC has received generous donations of FPGA chips from Xilinx Inc., under the Xilinx University Program. The EHTC has benefited from technology shared under open-source license by the Collaboration for Astronomy Signal Processing and Electronics Research (CASPER). The EHT project is grateful to T4Science and Microsemi for their assistance with Hydrogen Masers. This research has made use of NASA's Astrophysics Data System. We gratefully acknowledge the support provided by the extended staff of the ALMA, both from the inception of the ALMA Phasing Project through the observational campaigns of 2017 and 2018. We would like to thank A. Deller and W. Brisken for EHT-specific support with the use of DiFX. We thank Martin Shepherd for the addition of extra features in the Difmap software that were used for the CLEAN imaging results presented in this paper. We acknowledge the significance that Maunakea, where the SMA and JCMT EHT stations are located, has for the indigenous Hawaiian people. IMV acknowledges the use of LLuis Vives HPC resources of the University of Valencia.

Facilities: EHT, the Global mm VLBI Array, Atacama Large Millimeter Array, Chandra X-ray Observatory; Frontera supercomputer (Texas Advanced Computing Center), Puma Supercomputer (Arizona), Open Science Grid, CyVerse

Software: `BHAC`, `BHOSS`, `DIFMAP` (Shepherd 1997), `DMC`, `eht-imaging` (Chael et al. 2019), `foci`, `grmonty`, `hallmark`, `H-AMR`, `ipole`, KHARMA, `koral`, `mock-servation`, `SMILI`, THEMIS, `VIDA`, VisIt, numpy (van der Walt et al. 2011), scipy (Oliphant 2007), matplotlib (Hunter 2007).

Appendix A
Numerical Methods

A.1. Consistency of Radiative Transfer Simulations

Two studies have been undertaken within the EHT Collaboration to evaluate the consistency of radiative transfer codes.

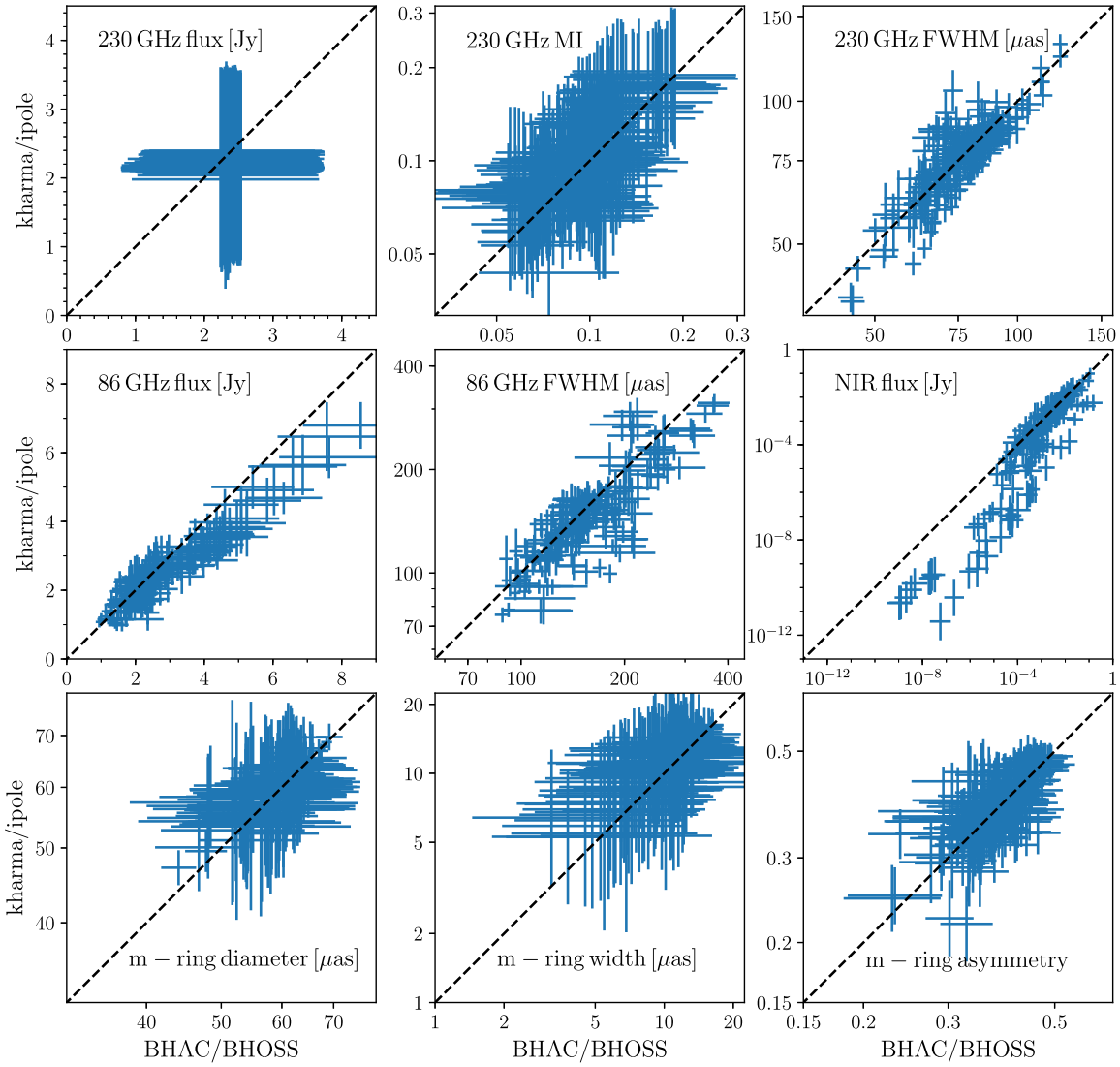

Figure 19. Correlation between `BHAC` and KHARMA models for nine model constraints. The horizontal axis is the constraint value from `BHAC/BHOSS`, and the vertical axis shows the constraint value from KHARMA/`ipole`. Each point corresponds to a single model, with the width of the distribution shown by the error bars. See text for details.

The first, Gold et al. (2020), evaluated the consistency between general relativistic ray-traced radiative transfer (GRRT) codes when tracing geodesics and when integrating the unpolarized radiative transfer equation. Gold et al. compare BHOSS and ipole, which are the two transfer codes used in this paper, and also compare to grtrans, raptor, odyssey, gray2, and raikou. Code consistency was found to be excellent, with sub-percent-level variations between codes when run with standard numerical parameters, i.e., without accuracy parameters tuned for consistency.

The second, B. Prather et al. (2022, in preparation), evaluates code performance when imaging GRMHD simulation output and when integrating the equations of polarized radiative transfer. Prather et al. include ipole, grtrans, odyssey, and raptor. Code consistency was also found to be excellent.

Uncertainty in the radiative transfer calculation is therefore unlikely to contribute significantly to the model error budget.

A.2. GRMHD Simulations Consistency and Convergence

As evident in Table 1, the thermal models have been calculated for an identical parameter space from two different codes, namely, KHARMA and BHAC for the GRMHD simulations and ipole and BHOSS codes for the GRRT calculations. This allows us to perform an in-depth comparison between the different numerical methods used in this work, in addition to the EHTC code comparison projects (Porth et al. 2019; Gold et al. 2020).

In Figure 19 we show the correlation between the thermal KHARMA and BHAC models for constraints where we have predictions from both models. The top row shows, from left to right, the 230 GHz flux density, M_3, and the 230 GHz image size obtained from image moments. Since we normalize the 230 GHz images to an average flux of 2.4 Jy within a time window of 5000 M (28.5 hr for Sgr A*), the scatter around this value is small. The deviation from an ideal correlation reflects the precision and number of GRMHD snapshots included during normalization procedure.

The correlation in M_3 spreads over $\Delta M_3 = 0.75$, which serves as a measure of intracode (e.g., MAD vs. SANE accretion) and intercode (BHAC vs. KHARMA) differences. Despite these differences, the models show a strong correlation throughout the investigated models and parameter space.

We also find a strong correlation between models and codes for the image size computed from image moments, i.e., second-moment analysis.

The middle row presents the correlation plots for the 86 GHz flux density (left), the 86 GHz image size using second moments (middle), and the NIR flux (right). The 86 GHz flux and 86 GHz image size exhibit a shift toward larger values for the BHAC models. This difference can be explained by the larger field of view used for the BHAC models at 86 GHz during the radiative transfer calculations. Thus, more extended structure and therefore a larger total flux are included in the BHAC models. This affects mainly models with large inclinations $i \geqslant 70^\circ$ and jet-dominated emission models ($R_{\rm high} \geqslant 40$).

The NIR fluxes show a tight correlation over four orders of magnitude and systematically larger flux for the BHAC models for low NIR fluxes ($\log_{10}(\mathrm{NIR/Jy}) < -7$). These fluxes are far below the NIR constraints of ~ 1 mJy, and therefore they do not affect the passing or failing of the models. In the thermal models the NIR flux is generated from the tail of the eDF and is thus very sensitive to the electron temperature. Small differences in the distribution and value of the electron temperature between the two codes explain the observed decorrelation at very low NIR flux.

The correlation between models for the m-ring parameters is presented in the third row of Figure 19. The correlation of the diameter of the m-ring is plotted in the left panel. The spread covers nearly the same extent as the 230 GHz image size (top row, right panel); however, the scatter in the correlation is larger. The same is true for the width of the m-ring (middle panel in the last row of Figure 19). Compared to the diameter and width of the m-ring, the asymmetry of the m-ring is less correlated (right panel). Notice that horizontal and vertical limits in the asymmetries occur because the parameter hits the boundary of the allowed range, which is 0.5.

The smaller correlation of the m-ring parameters as compared to the other parameters presented in Figure 19 is a consequence of the noisy nature of the m-ring fits. Still, the distributions are quite symmetric under reflection across the diagonal, so the models are at least not biased with respect to each other. Notice also that these plots do not capture all the information that is contained in the distribution of m-ring parameters, just the central value.

We are somewhat surprised by the strength of the correlations seen in Figure 19. The range of each constraint is substantially larger than the width of the correlation, so the variations between models are real, detectable, and reproducible with independent codes. The question of the origin of the systematic offsets between models for some constraints (e.g., in the NIR) is interesting but beyond the scope of this paper.

Appendix B
Variability of GRMHD Models

Nearly all models fail to recover the variability of Sgr A* in 230 GHz flux density as measured by M_3. In this appendix we discuss and dismiss four possible causes for this variability excess.

B.1. Effect of Resolution

For the 50% change in resolution considered in the comparison shown in the preceding appendix (between KHARMA and BHAC simulations) we find no evidence for systematic changes in M_3 with resolution. This is not a large range in resolution, however, and much higher resolution simulations (Ripperda et al. 2020, 2022; Nathanail et al. 2021) show the emergence of qualitatively new structures (plasmoids) in current sheets that could affect 230 GHz variability. A deeper study of the resolution dependence of variability is clearly warranted but is beyond the scope of this paper.

B.2. Simulation Duration

The fiducial models are evolved for $\sim 30{,}000\, GM/c^3$. Figure 20 compares M_3 distributions from a fiducial KHARMA simulation to a koral model with similar parameters that was evolved and imaged for approximately three times longer. The M_3 distributions have similar mean and standard deviation regardless of time interval chosen for comparison.

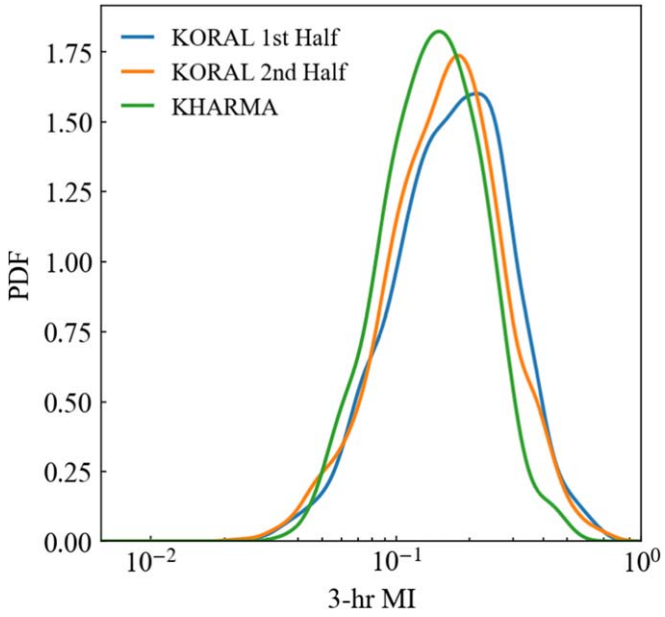

Figure 20. Distribution of M_3 from `koral` models, divided between the first and second half of the simulation, and from the fiducial KHARMA models. We choose the models that are at similar points in the parameter space, limiting the comparison to spin −0.9, −0.5, 0.0, and 0.9 over all inclinations for the `koral` models and MAD, $R_{\rm high}$ 40, spin −0.94, −0.5, 0.0, and 0.94 for the KHARMA models.

B.3. Effect of R_{low}

The $R_{\rm high}$ prescription (Equation (13)) has three free parameters: $R_{\rm high}$, $R_{\rm low}$, and $\beta_{\rm crit}$. In the main text the $R_{\rm high}$ parameter is varied while $R_{\rm low}$ and $\beta_{\rm crit}$ are set to unity.

The $R_{\rm low}$ parameter determines the electron temperature in regions of low β, i.e., in and near the funnel. Increasing $R_{\rm low}$ mimics rapid electron cooling. We are particularly interested in the effect of increasing $R_{\rm low}$ on M_3.

Figure 21 shows the M_3 distribution for a set of four KHARMA models with four values of $R_{\rm low}$ (1, 2, 5, and 10). Evidently the M_3 distribution does not exhibit a clear trend with $R_{\rm high}$ and is still inconsistent with the observed distribution even at $R_{\rm low} = 10$.

B.4. Effect of Self-consistent Electron Heating

Ressler et al. (2015) provide a formulation to model electron thermodynamics during the fluid evolution. Numerical dissipation at the grid scale sources entropy generation and is used to heat the electrons based on a microphysical, subgrid heating prescription. Local fluid and electromagnetic variables are used to compute the electron entropy, which, along with the ideal gas equation of state, can be converted into a temperature Θ_e. This approach allows computing the electron temperature at each time step of the simulation rather than post-processing, as is done in the $R_{\rm high}$ and critical-β prescriptions.

We consider three subgrid heating models that prescribe the partition of dissipated energy into electrons and ions. Howes (2010) computed the ratio of ion to electron heating due to dissipation of Alfvénic turbulent cascade, while Werner et al. (2017) and Rowan et al. (2017) considered magnetic reconnection as the source of energy dissipation at subgrid scales. These studies provide approximate fitting formulae for the ion-to-electron heating rate Q_i/Q_e based on local ion-to-electron temperature ratio T_i/T_e and local magnetic field strength—parameterized by σ or β.

We use a subset of the simulations analyzed in Dexter et al. (2020). These include MAD and SANE accretion flows at spins $a_* = 0, +1/2, +15/16$. We compute the 3 hr modulation index M_3, over the time interval 5000–10,000 GM/c^3. The average M_3 values are comparable to similar $R_{\rm high}$ models, with SANE reconnection models exhibiting a slightly reduced variability as compared to the corresponding turbulent heating models. However, the M_3 distribution is still inconsistent with the historical data.

B.5. Effect of Fluid Adiabatic Index

We expect the ions and electrons in hot accretion flows to be thermally decoupled and the resulting plasma to be two-temperature (Shapiro et al. 1976; Quataert 1998; Sadowski et al. 2016; Chael et al. 2018; Ryan et al. 2018). The electrons are relativistic and can be modeled as a fluid with an adiabatic index $\Gamma_e = 4/3$, while the ions are nonrelativistic with adiabatic index $\Gamma_i = 5/3$.

The adiabatic index of the fluid assumes a value between Γ_e and Γ_i dictated by the thermodynamics of the ions and electrons (see Figure 4 in Sadowski et al. 2016). If the electrons and ions have equal temperature, then in the relativistic electron/nonrelativistic ion regime the fluid adiabatic index is 13/9.

Our simulations are not fully consistent in their treatment of the adiabatic index. All use a fixed $\Gamma_{\rm ad}$, but some set $\Gamma_{\rm ad} = 4/3$ while others use 13/9 or 5/3.

Two-temperature simulations can self-consistently evolve adiabatic indices of electrons and ions and compute the net fluid adiabatic index with contributions from both species (Sadowski et al. 2016). These two-temperature simulations often show variation of the adiabatic index with polar angle, with the fluid energy dominated by hot electrons near the poles ($\Gamma = 4/3$) and by cooler ions and electrons in the midplane ($\Gamma = 5/3$).

We evaluate the effect of $\Gamma_{\rm ad}$ on light-curve variability by comparing M_3 for thermal, GRMHD simulations with varying $\Gamma_{\rm ad}$. This includes MAD models with $\Gamma_{\rm ad} = 13/9$ (see Section B.2 and Narayan et al. 2022) and SANE models with $\Gamma_{\rm ad} = 5/3$. The models exhibit light-curve variability similar to the fiducial models, and all have M_3 distributions that are inconsistent with the historical data.

Appendix C
Pass/Fail Plots

The full set of constraint results for the fiducial models is presented below in graphical form.

We start with the EHT constraints. Figure 22 shows the 230 GHz 2nd moment constraint and Figure 23 shows the null location constraint. Figures 24–26 show m-ring diameter, width, and asymmetry constraints, respectively. Figure 27 combines all the EHT constraints listed above.

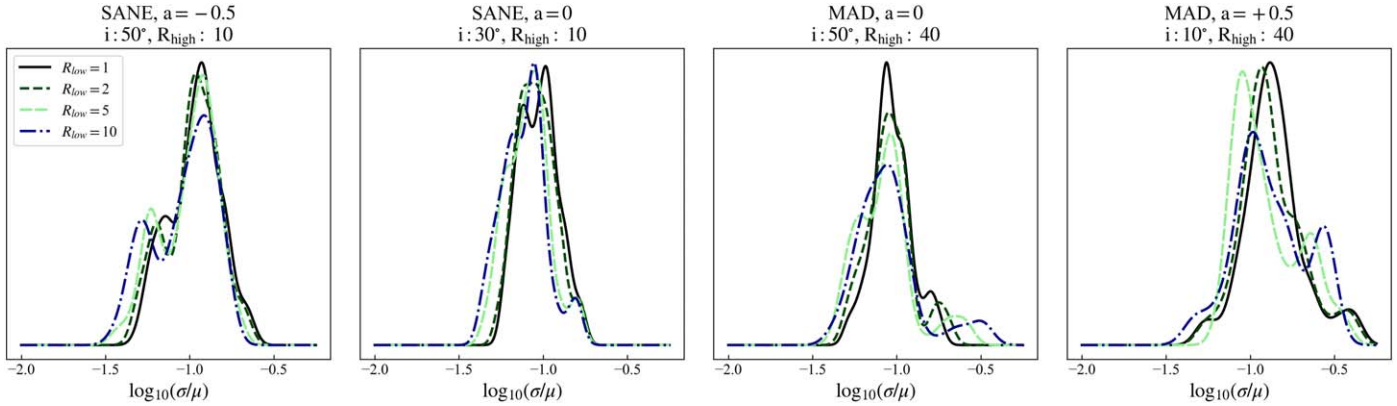

Figure 21. Modulation index computed over 3 hr intervals M_3 for a subset of the thermal models (KHARMA data sets). For this analysis, we considered the 25,000–30,000 GM/c^3 time interval.

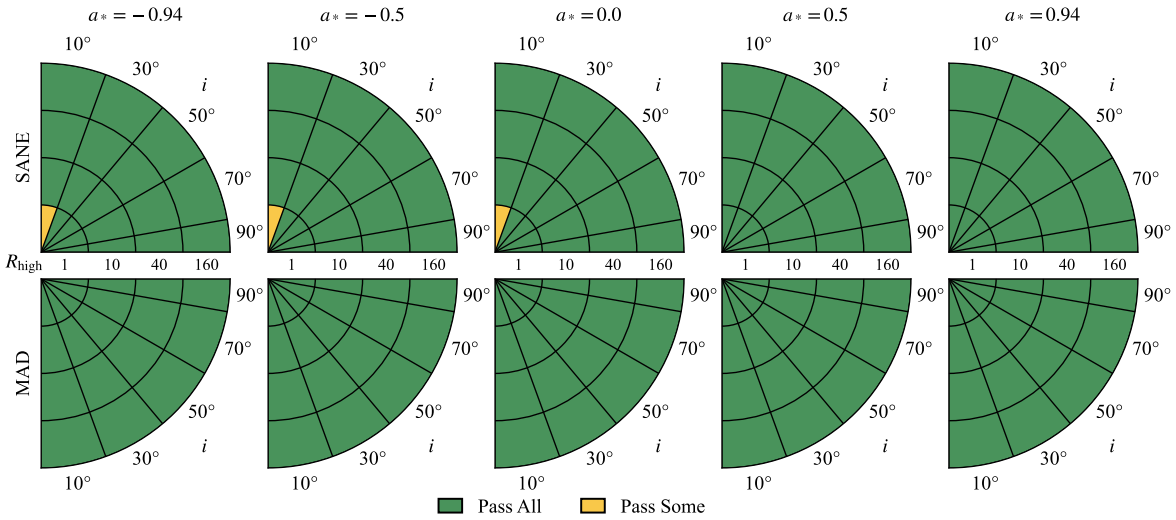

Figure 22. Second-moment constraint. Green indicates that the KHARMA, BHAC, and H-AMR models pass, yellow that one or two of the fiducial models fail, and red that all three fail.

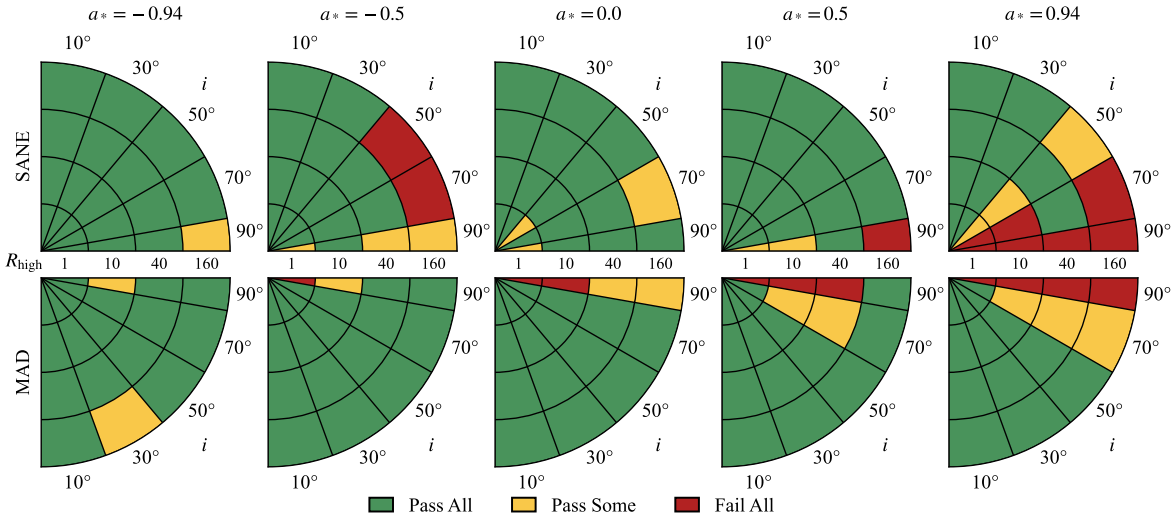

Figure 23. Null location constraint. Green indicates that the KHARMA, BHAC, and H-AMR models pass, yellow that one or two of the fiducial models fail, and red that all three fail.

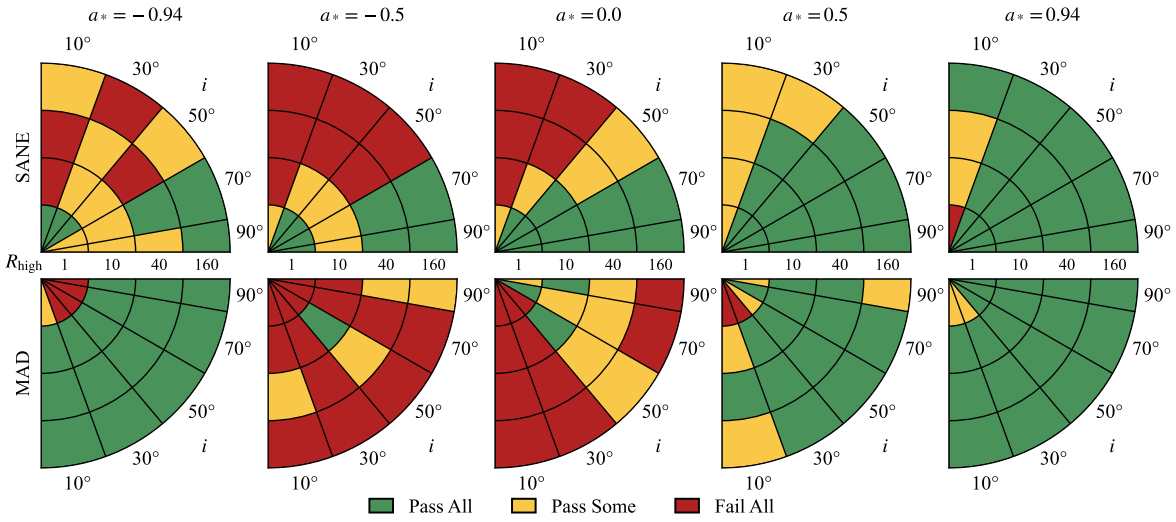

Figure 24. M-ring diameter constraints. Green indicates that the KHARMA, BHAC, and H-AMR models pass, yellow that one or two of the fiducial models fail, and red that all three fail.

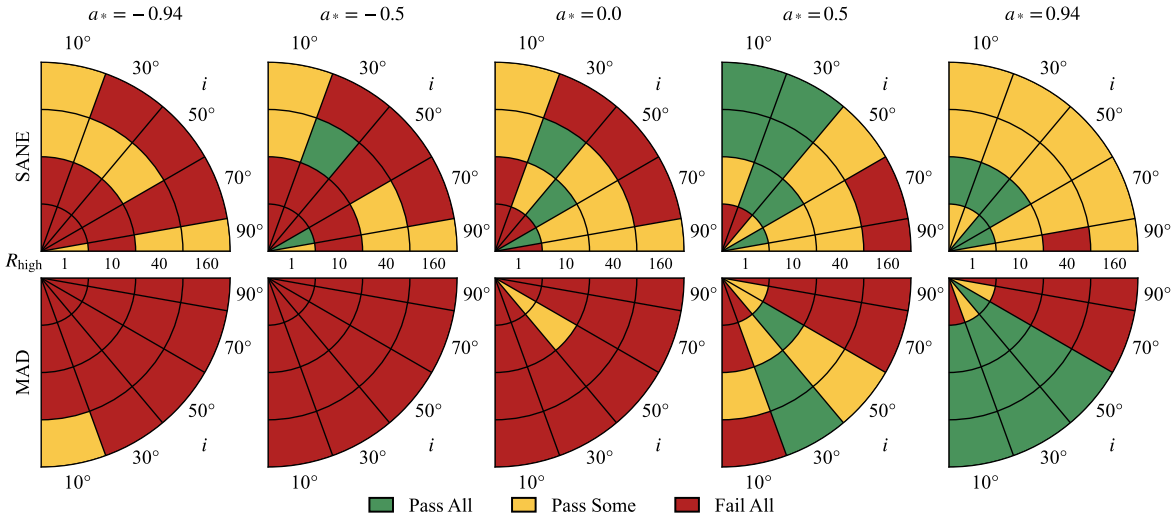

Figure 25. M-ring width constraints. Green indicates that the KHARMA, BHAC, and H-AMR models pass, yellow that one or two of the fiducial models fail, and red that all three fail.

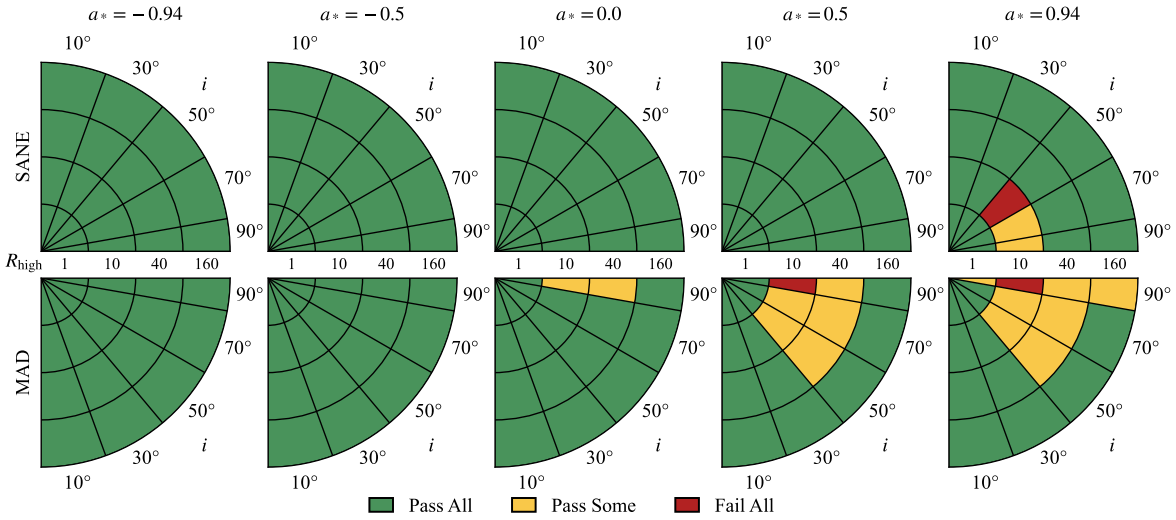

Figure 26. M-ring asymmetry constraints. Green indicates that the KHARMA, BHAC, and H-AMR models pass, yellow that one or two of the fiducial models fail, and red that all three fail.

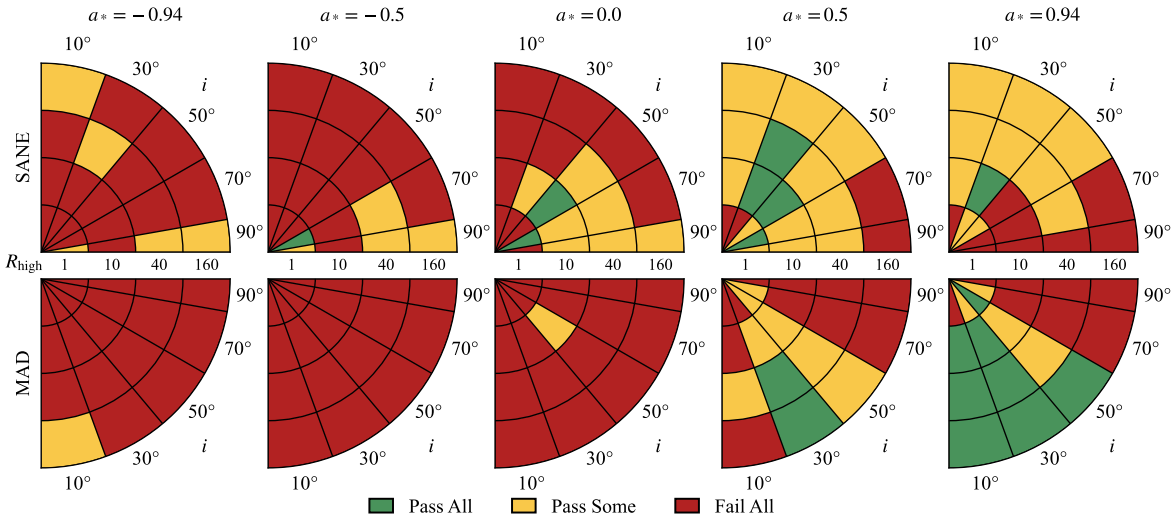

Figure 27. Combined EHT constraints. Green indicates that the KHARMA, BHAC, and H-AMR models pass, yellow that one or two of the fiducial models fail, and red that all three fail.

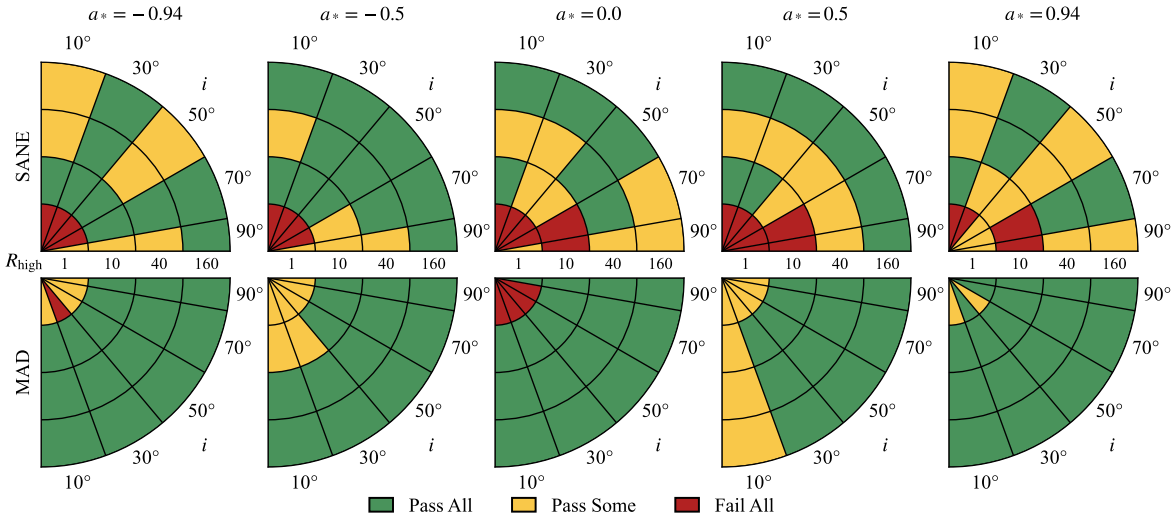

Figure 28. 86 GHz flux constraints. Green indicates that the KHARMA, BHAC, and H-AMR models pass, yellow that one or two of the fiducial models fail, and red that all three fail.

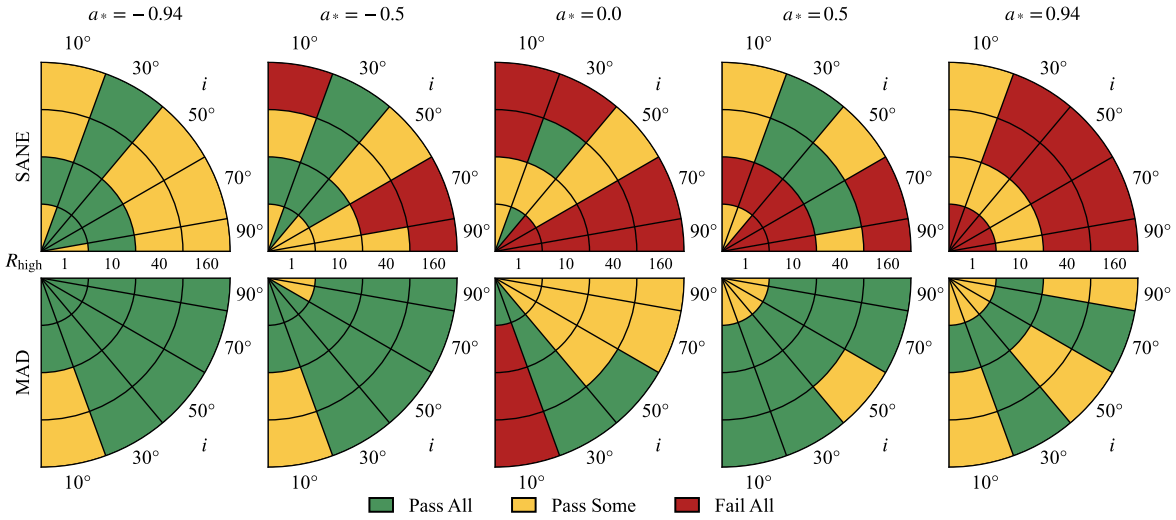

Figure 29. 86 GHz size constraints. Green indicates that the KHARMA, BHAC, and H-AMR models pass, yellow that one or two of the fiducial models fail, and red that all three fail.

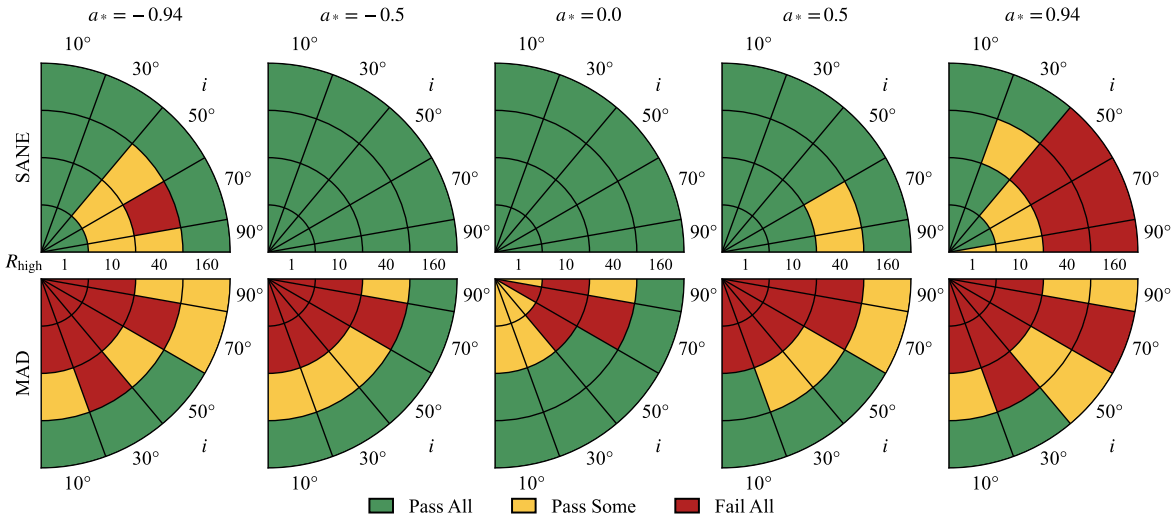

Figure 30. 2.2 μm flux constraints. Green indicates that the KHARMA, BHAC, and H-AMR models pass, yellow that one or two of the fiducial models fail, and red that all three fail.

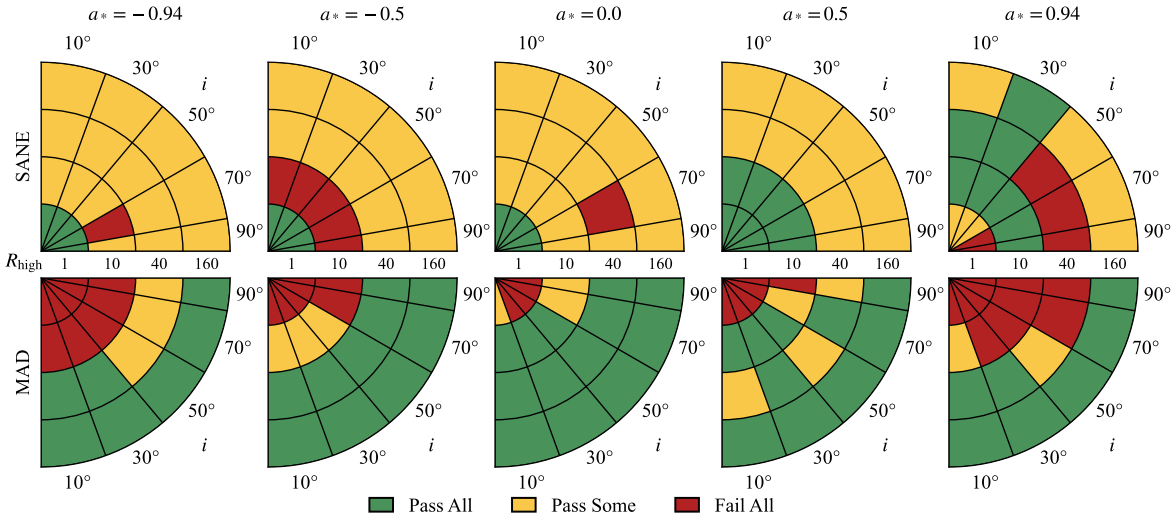

Figure 31. X-Ray luminosity constraints. Green indicates that the KHARMA, BHAC, and H-AMR models pass, yellow that one or two of the fiducial models fail, and red that all three fail.

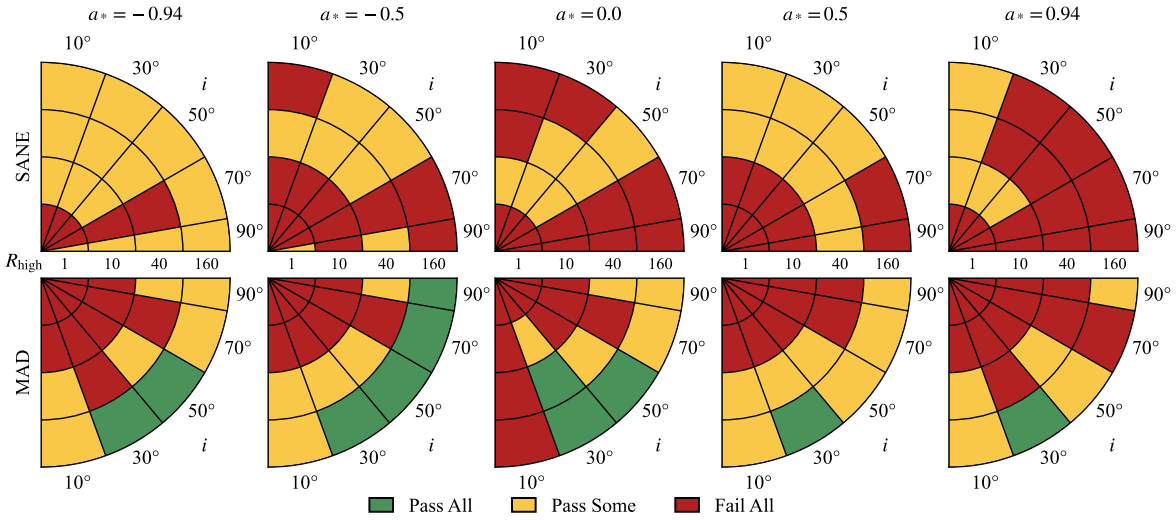

Figure 32. Combined non-EHT constraints. Green indicates that the KHARMA, BHAC, and H-AMR models pass, yellow that one or two of the fiducial models fail, and red that all three fail.